

# Symmetry-adapted tight-binding calculations of the totally symmetric $A_1$ phonons of single-walled carbon nanotubes and their resonant Raman intensity

Valentin N. Popov\*, Philippe Lambin

*Laboratoire de Physique du Solide, Facultés Universitaires Notre-Dame de la Paix, 61 rue de Bruxelles, B-5000 Namur, Belgium*

Available online 27 September 2006

## Abstract

The atomistic calculations of the physical properties of perfect single-walled carbon nanotubes based on the use of the translational symmetry of the nanotubes face increasing computational difficulties for most of the presently synthesized nanotubes with up to a few thousand atoms in the unit cell. This difficulty can be circumvented by use of the helical symmetry of the nanotubes and a two-atom unit cell. We present the results of such symmetry-adapted tight-binding calculations of the totally symmetric  $A_1$  phonons (the RBM and the  $G$ -band modes) and their resonant Raman intensity for several hundred nanotubes.

In particular, we show that (1) the frequencies and the resonant Raman intensity of the RBM and the  $G$ -band modes show diameter and chirality dependence and family patterns, (2) the strong electron– $A_1^{\text{LO}}$  phonon interactions in metallic nanotubes lead to Kohn anomalies at the zone center, (3) the  $G$ -band consists of a subband due to  $A_1^{\text{LO}}$  phonons of semiconducting tubes centered at  $\sim 1593 \text{ cm}^{-1}$ , a subband of  $A_1^{\text{TO}}$  phonons at  $\sim 1570 \text{ cm}^{-1}$ , and a subband of  $A_1^{\text{LO}}$  phonons of metallic tubes at  $\sim 1540 \text{ cm}^{-1}$ . The latter prediction confirms previous theoretical results but disagrees with the commonly adopted assignment of the  $G$ -band features.

© 2006 Elsevier B.V. All rights reserved.

PACS: 61.46.Fg; 63.22.+m; 78.30.Na

Keywords: Nanotube; Phonons; Raman scattering

## 1. Introduction

Recent progress in the synthesis of single-wall carbon nanotube and their observation by combined microscopic and spectroscopic techniques has made the need of precise theoretical modeling more acute than ever [1–3]. The industrial application of carbon nanotubes requires their accurate characterization by measurements and theoretical predictions, and further on, the detailed knowledge of the properties of the individual nanotubes. The theoretical advance in this direction is hindered by the wide variety of the nanotube types and the necessity in most cases to carry out calculations for each of these types separately. The main problem before the atomistic study of the nanotube properties is the relatively low symmetry of the tubes

resulting in normally large unit cells. This major problem can successfully be overcome by considering the helical (screw) symmetry of the nanotube that allows reducing the large unit cell to smaller repeat units consisting of two atoms only [4]. This symmetry-based approach has been applied before to helical polymers with only one type of screw operations. In nanotubes, the entire nanotube can be constructed by means of two types of screw operations and a two-atom repeat unit (or two-atom unit cell). This approach has been successfully used in force-constant and tight-binding lattice-dynamical studies of nanotubes as well as electronic band structure calculations. The knowledge of the phonon dispersion and the band structure is a starting point for further work on the electron–phonon interactions, which are basic for many phenomena in physics, e.g., electronic transport, resonant Raman scattering of light, etc. The introduction of the helical symmetry in phenomenological and tight-binding models is straightforward but

\*Corresponding author. Tel.: +32 81 72 54 85; fax: +32 81 72 47 07.  
E-mail address: [valentin.popov@fundp.ac.be](mailto:valentin.popov@fundp.ac.be) (V.N. Popov).

it is accompanied by major difficulties for ab-initio schemes.

Here we present recent results on the calculation of the frequencies of the totally symmetric zone-center phonons and the resonant Raman intensity of these phonons. We show that the calculations within a well-tuned nonorthogonal tight-binding model for all nanotubes of practical interest give valuable information for the diameter and chirality dependence of these quantities. The obtained results reveal that some of the widely used approximations are not valid for all tubes and all cases. The paper is organized as follows. Section 2 gives brief theoretical insight on the incorporation of the helical symmetry in lattice-dynamical and band-structure models. Next, the electron–phonon matrix element, necessary for phonon and resonant Raman intensity calculations, is derived. Section 3 presents results and discussion on the zone-center phonon frequencies and the resonant Raman intensity for several hundred nanotubes. The paper ends with conclusions.

## 2. Theoretical part

The atomistic calculations for phonons and electrons in infinite periodic structures are facilitated by the use of the translational symmetry of the structure. In cases, where the problem is transformed to a matrix one, the rank of the matrix to be diagonalized is proportional to the number of the atoms in the primitive unit cell of the structure. The large number of atoms in the unit cell may hinder the calculations and even make them impossible. Such situation is normally met in carbon nanotubes, where the number of carbon pairs in the unit cell may be as large as several thousand for the usually synthesized nanotubes. This problem can be circumvented by using the helical symmetry of the nanotubes and the corresponding two-atom repeat unit (or two-atom unit cell). This approach requires starting from properly symmetrized phonon polarization vectors and electronic basis functions. We shall exemplify this procedure in the case of a force-constant model of the lattice dynamics of nanotubes and shall extend it to tight-binding models for electronic band structure and phonon dispersion calculations. The symmetry-based approach can easily be extended to encompass other elementary excitations in the nanotubes, such as excitons, polarons, etc. Before proceeding, we note that a nanotube can be obtained by rolling up of an infinite strip of graphene along a lattice vector into a seamless cylinder and can uniquely be characterized by the pair of indices  $(L_1, L_2)$  of the lattice vector. Such a tube has a diameter  $d$ , a chiral angle  $\theta$ , which is the angle between the lattice vector and the nearest zigzag of carbon atoms, and contains  $N$  carbon pairs in the unit cell.

First, we consider a force-constant model of the lattice dynamics of nanotubes [5]. Let  $\mathbf{R}(\mathbf{l}\kappa)$  be the equilibrium position vector of the  $\kappa$ th atom in the  $l$ th two-atom unit cell. For small displacements  $\mathbf{u}(\mathbf{l}\kappa)$  of the atoms from their

equilibrium positions, the potential energy of the distorted tube can be expanded in series of  $\mathbf{u}(\mathbf{l}\kappa)$  up to second order. Using the Lagrangian of the tube, one can readily write the equations of motion as a system of an infinite number of linear ordinary differential equations for the displacement components. The problem can be reduced to a finite rank matrix eigenvalue problem by assuming a solution for the atomic displacements in the form of a traveling wave with a two-component wavevector. The two components of the latter are not independent and can be determined by imposing the rotational boundary condition and the translational periodicity condition on the atomic displacements. This leads to the following form of the atomic displacements:

$$u_\alpha(\mathbf{l}\kappa) = \frac{1}{\sqrt{m_C}} \sum_{\beta} S_{\alpha\beta}(\mathbf{l}) e_{\beta}(\kappa|ql) \exp i[\alpha(\mathbf{l})l + z(\mathbf{l})q - \omega t]. \quad (1)$$

Here  $m_C$  is the carbon atom mass,  $e_{\beta}$  the phonon polarization vector,  $k$  the one-dimensional wavevector of the tube ( $-\pi \leq q < \pi$ ),  $l$  the azimuthal quantum number ( $l = 0, 1, \dots, N-1$ ) and  $\omega$  the phonon frequency.  $\alpha(\mathbf{l})$  and  $z(\mathbf{l})$  determine the position of the  $l$ th cell around the tube circumference and along the tube axis, respectively.  $S_{\alpha\beta}$  is a rotation matrix, rotating  $e_{\beta}$  from the zeroth cell to the  $l$ th cell, preserving the relative orientation of the polarization vector with respect to the tube.

The substitution of Eq. (1) in the equations of motion gives the system of six linear equations:

$$\omega^2(ql) e_{\alpha}(\kappa|ql) = \sum_{\kappa'\beta} D_{\alpha\beta}(\kappa\kappa'|ql) e_{\beta}(\kappa'|ql). \quad (2)$$

The dynamical matrix  $D_{\alpha\beta}$  is expressed through the force constants  $\Phi_{\alpha\beta}$  as

$$D_{\alpha\beta}(\kappa\kappa'|ql) = \frac{1}{m_C} \sum_{\Gamma\gamma} \Phi_{\alpha\gamma}(\mathbf{0}\kappa, \mathbf{l}\kappa') S_{\gamma\beta}(\mathbf{l}) \exp i[\alpha(\mathbf{l})l + z(\mathbf{l})q]. \quad (3)$$

The equations of motion, Eq. (2), give the phonon frequencies  $\omega(qlj)$  and eigenvectors  $e_{\beta}(\kappa|qlj)$ ,  $j = 1, 2, \dots, 6$ . For each  $q$ , there are  $3N$  phonons but the number of different frequencies can be smaller because of degeneracy. Under the operations of the screw subgroup of the tube, the eigenvectors with  $l = 0$  or  $(N/2) - 1$  transform into themselves, while for the other values of  $l$ , the eigenvectors with  $l$  and  $N - l$  form the basis of two-dimensional group representations.

Similarly, we shall illustrate the application of the symmetry-based approach in the tight-binding model of the electronic band structure of the nanotubes [6]. In this model, each atom is ascribed a certain number of hydrogen-like (Slater or Gaussian) orbitals and the one-electron basis wavefunctions  $\varphi$  are expanded as linear combinations of all orbitals with a two-component wavevector. As above, the two components can be determined by imposing the rotational boundary condition

and the translational periodicity condition on the basis wavefunctions. Eventually, they can be cast in the form

$$\varphi_{klr} = \frac{1}{\sqrt{N}} \sum_{\mathbf{r}'} \exp i[\alpha(\mathbf{l})l + z(\mathbf{l})k] T_{rr'}(\mathbf{l}) \chi_{r'}[\mathbf{R}(\mathbf{l}\kappa) - r]. \quad (4)$$

The orbitals  $\chi$  are centered on atoms with position vectors  $\mathbf{R}(\mathbf{l}\kappa)$ . The index  $r = 1, \dots, 2s$  runs over the orbitals of the two atoms in the unit cell ( $s = 1$  for a model with a single  $\pi$  orbital per atom, the so-called  $\pi$ TB model;  $s = 4$  for the all-valence tight-binding model with four orbitals per atom). The matrices  $T_{rr'}$  perform rotation in the space of the orbitals from the zeroth cell to the  $l$ th unit cell, preserving the orientation of the orbitals relative to the tube surface.

The one-electron wavefunction is expanded in the basis functions with expansion coefficients  $c_{klr}$ :

$$\psi_{kl} = \sum_r c_{klr} \varphi_{klr}. \quad (5)$$

The substitution of Eq. (5) in the one-electron Schrödinger equation reduces the electronic problem to the matrix eigenvalue one:

$$\sum_{r'} H_{klr'r} c_{klr'} = E_{kl} \sum_{r'} S_{klr'r} c_{klr'}. \quad (6)$$

Here

$$H_{klr'r} = \sum_{\mathbf{r}''} \exp i[\alpha(\mathbf{l})l + z(\mathbf{l})k] H_{rr''}(\mathbf{l}) T_{r''r'}(\mathbf{l}), \quad (7)$$

and

$$S_{klr'r} = \sum_{\mathbf{r}''} \exp i[\alpha(\mathbf{l})l + z(\mathbf{l})k] S_{rr''}(\mathbf{l}) T_{r''r'}(\mathbf{l}), \quad (8)$$

are expressed through the matrix element of the one-electron Hamiltonian  $H_{rr'}(\mathbf{l})$ , and the overlap matrix element  $S_{rr'}(\mathbf{l})$  between two orbitals, centered on an atom at the origin and an atom in the  $l$ th unit cell. The solutions of Eq. (5) are the electron eigenenergies  $E_{klm}$  and the expansion coefficients  $c_{klmr}$  ( $m = 1, \dots, 2s$ ). For each  $k$ , there are  $2sN$  electronic states but the number of different eigenenergies is smaller because of degeneracy. As above, only nondegenerate and doubly-degenerate energy levels are possible. The tubes can be metallic (or tiny-gap semiconductors) or semiconducting if the residual of the division of  $L_1 - L_2$  by 3 is 0 or 1 and 2. For this reason, the metallic tiny-gap semiconducting tubes are also referred to as Mod0 tubes and the semiconducting tubes are called Mod1 and Mod2 tubes.

In some more sophisticated tight-binding models that include pairwise interatomic interactions, one can calculate the total energy of the system and perform structural relaxation. This is mandatory for phonon calculations, where one should know the equilibrium state of the system. We note that the independent-electron approximation may not be adequate for some phenomena and then one should resort to a more complicated description in terms of excitons. However, we shall use this approximation,

bearing in mind that the symmetry-based approach can be extended to encompass excitons as well.

Some phenomena in nanotubes can be modeled separately by phonons (specific heat, thermal conductance, nonresonant Raman intensity, etc.) or electrons (optical absorption, ballistic electronic transport, etc.). However, the majority of the phenomena in nanotubes require the explicit account of two or more elementary excitations and their interactions in the presence of external fields, hydrostatic pressure, thermal gradient, etc. For example, electrons, excited to higher conduction bands will be scattered by phonons to lower bands. The electronic transport is determined by intraband scattering of electrons from acoustic and optical phonons. In the resonant Raman scattering, an electron is excited to a real or a virtual state, scattered to a lower real or virtual state, and finally the electron recombines with a hole. In all cases, the fundamental quantity, describing the electron–phonon interaction is the matrix element of the interaction Hamiltonian.

The electron–phonon matrix element for scattering of an electron from an initial state ( $klm$ ) to a final state ( $k'l'm'$ ) with emission/absorption of a phonon ( $q\lambda j$ ) can be calculated within the nonorthogonal tight-binding model using time-dependent perturbation theory. The perturbed wavefunction is presented as a linear combination of the stationary wavefunctions  $\psi_{klm}(\mathbf{r})$  with time-dependent expansion coefficients  $a_{klm}(t)$ . This expansion is substituted in the time-dependent Schrödinger equation for the perturbed Hamiltonian  $\hat{H} + \delta\hat{H}$ . Considering  $a_{klm}(t)$  as a first-order quantity in the perturbation  $\delta\hat{H}$ , the first-order equation reads

$$i\hbar \dot{a}_{klm} = \sum_{klm} M_{k'l'm',klm} a_{klm}. \quad (9)$$

The matrix element  $M_{k'l'm',klm}$  is given by

$$M_{k'l'm',klm} = \sum_{rr'} c_{k'l'm'r}^* (\delta H_{klr'r} - E_{klm} \delta S_{klr'r}) \times c_{klmr} e^{-i(E_{k'l'm'} - E_{klm})t/\hbar}, \quad (10)$$

and  $\delta H_{klr'r}$  and  $\delta S_{klr'r}$  are perturbations of  $H_{klr'r}$  and  $S_{klr'r}$  due to the phonon. Using second-quantization representation of the atomic displacements, one readily obtains the electron–phonon matrix element as

$$M_{k'l'm',klm} = \left( \frac{\hbar}{2Nm_C \omega_{q\lambda j}} \right)^{1/2} M_{k'l'm',klm}, \quad (11)$$

where

$$M_{k'l'm',klm} = \sum_{rr'} c_{k'l'm'r}^* (M'_{k'l'r'r} - M_{klr'r}) c_{klmr}. \quad (12)$$

The matrix element  $M'_{k'l'r'r}$  is

$$M'_{k'l'r'r} = \sum_{l''} e^{i[\alpha(\mathbf{l})l'' + z(\mathbf{l})k'']} [\nabla H_{rr''}(\mathbf{l}) - E_{klm} \nabla S_{rr''}(\mathbf{l})] \times T_{r''r'}(\mathbf{l}) \cdot S(\mathbf{l}) e_{q\lambda j}(\kappa'), \quad (13)$$

and  $M_{klr'r}$  is given by a similar expression with  $l' \rightarrow l$ ,  $k' \rightarrow k$ , and  $\kappa \rightarrow \kappa'$ . The gradient is with respect to  $\mathbf{R}(\mathbf{0}\kappa) - \mathbf{R}(\mathbf{l}\kappa')$ . We

note that for the process of electron scattering, there is conservation of energy ( $E_{k'l'm'} = E_{klm} \pm \hbar\omega_{\pm q \pm \lambda j}$ ), wave-vector ( $k = k' - q$ ), and azimuthal quantum number ( $l = l' - \lambda$ ). Finally, the electron–phonon interaction Hamiltonian can be written as

$$\hat{H}_{e-ph} = \sum_{klm} M_{k'l'm',klm} c_{k'l'm'}^+ c_{klm} (a_{q\lambda j} + a_{-q-\lambda j}^+), \quad (14)$$

where  $c^+$  and  $c$ , and  $a^+$  and  $a$  are the creation and annihilation operators for electrons and phonons, respectively.

We consider two cases, in which the electron–phonon interactions play important role. The resonant Raman scattering of light from phonons is a complex process of absorption of a photon with energy  $E_L$  and creation of an electron–hole pair, scattering of the electron/hole by an optical phonon with energy  $E_o = \hbar\omega_o$ , and annihilation of the electron–hole pair with emission of a photon with energy  $E_S$ . The Raman intensity for the most intense Stokes process can be written as [7]

$$I(E_L, E_o) = A \left| \frac{1}{L} \sum_{cv} \frac{p_{cv}^S M_{cv} p_{cv}^{L*}}{(E_L - E_{cv} - i\gamma_e)(E_S - E_{cv} - i\gamma_e)} \right|^2. \quad (15)$$

Here  $A = C(E_S/E_L)^2(n+1)$  with  $C$  being a constant,  $n$  is the phonon Bose–Einstein factor,  $L$  the tube length, and  $\gamma_e$  the excited state width.  $E_{cv}$  is the energy difference for a given pair of valence ( $v$ ) and conduction ( $c$ ) bands and the summation is over all  $k$ -vectors and all pairs of  $cv$  bands.  $p_{cv}$  is the component of the matrix element of the electron momentum in the direction of the incident/scattered photon polarization, calculated between the wavefunctions of a pair of valence and conduction bands.  $M_{cv}$  is the electron–phonon matrix element, given by the general expressions above, Eqs. (11)–(13). Further on, we shall consider only light polarization along the tube axis, when the matrix elements are nonzero only for pairs of bands with  $l = l'$ . Obviously, the intensity is resonantly enhanced for  $E_L$  and  $E_S$  close to a minimum of  $E_{cv}$ . Such minima correspond to the optical transition energies and will be denoted by  $E_{ii}$  ( $ii = 11, 22, \dots$ ).

The expression for the intensity can be simplified by noticing that most of the contribution to the sum in Eq. (13) comes from  $k$  points around a minimum of  $E_{cv}$ . We can pull the numerator out of the summation at the point of the minimum and carry out the remaining summation as integration. The obtained intensity is

$$I(E_L, E_o) = A' \left| \sum_{ii} J_{ii} F_{ii}(E_L, E_o) \right|^2, \quad (16)$$

where

$$J_{ii} = |p_{ii}|^2 M_{ii} \sqrt{m_{ii}^*}, \quad (17)$$

$$F_{ii}(E_L, E_o) = \frac{2}{\hbar\omega_o} \left( \frac{1}{\sqrt{E_L - E_{ii} - i\gamma_e}} - \frac{1}{\sqrt{E_S - E_{ii} - i\gamma_e}} \right), \quad (18)$$

$A' = C'(E_S/E_L)^2(n+1)$  with  $C'$  being a constant,  $m_{ii}^*$  the effective mass, and  $p_{ii}$  and  $M_{ii}$  are matrix elements at the minimum of  $E_{cv}$  for a given transition  $ii$ . It is clear that  $F_{ii}$  determines the resonance window, i.e., the range of laser energies, for which the intensity is noticeably different from zero, and  $J_{ii}$  determines the contribution of a given tube to the Raman intensity. Once  $J_{ii}$  are known for all tubes in a given range of tube diameters, one can easily calculate the Raman spectrum of a nanotube sample by summing up the intensity, Eq. (17), over all tube types with a weight factor proportional to the tube population in the sample.

Another application of the electron–phonon matrix elements is in the calculation of the phonon dispersion of nanotubes within the nonorthogonal tight-binding model. The dynamical matrix can be derived considering the change of the total energy of the tube due to a phonon up to second order in the perturbation.

### 3. Results and discussion

First, we calculated the zone-center phonons of all nanotubes in the diameter range 0.4–2.4 nm, which contains the usually synthesized nanotubes. Among these phonons, the zone center radial-breathing mode (RBM) and the Raman-active tangential optical modes (the  $G$ -band modes) play a most important role because of their high Raman intensity. Fig. 1, left, shows the dependence of the frequency  $\omega_{\text{RBM}}$  on the tube diameter  $d$ . The points can be fitted well with the power law  $\omega_{\text{RBM}} = 228/d$  ( $\omega_{\text{RBM}}$  in  $\text{cm}^{-1}$  and  $d$  in nm). The close look at the small-diameter region reveals a weak dependence on the tube chiral angle  $\theta$  that can be described well with a factor  $\cos(3\theta)$  (Fig. 1, inset). Two groups derived from Raman data  $\omega_{\text{RBM}} = (223/d) + 10$  for semiconducting tubes (S tubes) [8],  $\omega_{\text{RBM}} = (218/d) + 17$  for metallic and tiny-gap semiconducting tubes (M tubes) [8], and  $\omega_{\text{RBM}} = (214/d) + 18.7$  for both S and M tubes [9]. The presence of the additive term is generally explained with tube bundling and/or effect of environment, which are not accounted for in the present calculations.

The  $G$ -band of a nanotube sample consists of contributions of six tangential modes of symmetry  $2A_1 + 2E_1 + 2E_2$  in chiral tubes and three tangential modes  $A_{1g} + E_{1g} + E_{2g}$  in armchair and zigzag tubes. These modes are polarized either almost along the tube axis (LO modes) or along the tube circumference (TO modes). Calculations within a force-constant model show that the LO and TO frequencies for each symmetry species lie on two separate strips versus tube diameter. The present tight-binding results reveal that the strong electron– $A_1^{\text{LO}}$  phonon interactions in  $M$  tubes lead to softening of the  $A_1^{\text{LO}}$  mode frequencies. Thus, there are three strips of points instead of two, arising from  $A_1^{\text{LO}}$

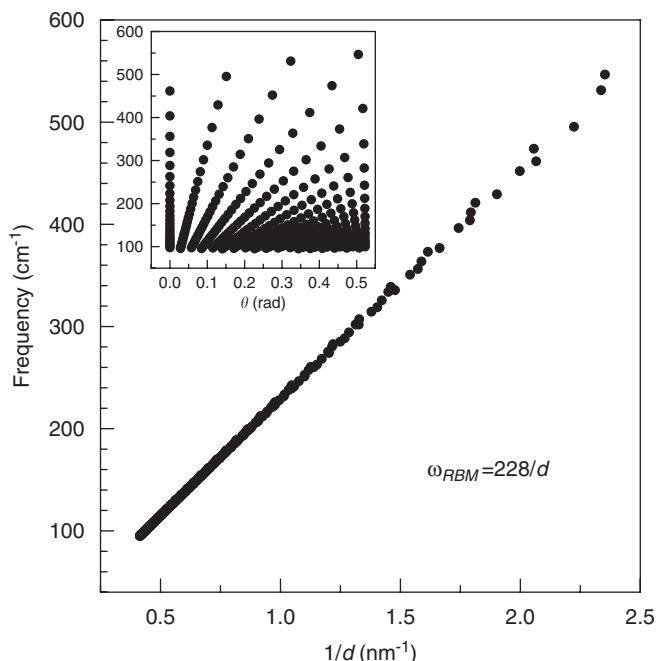


Fig. 1. The calculated frequency of the RBM for all nanotubes in the diameter range 0.4–2.4 nm. The data lie approximately on a straight line given by the simple power law  $228/d$  ( $d$  is the tube diameter in nm). The inset shows the chirality dependence of the frequency, which is well described by a factor  $\cos(3\theta)$ ,  $\theta$  being the chiral angle in rad.

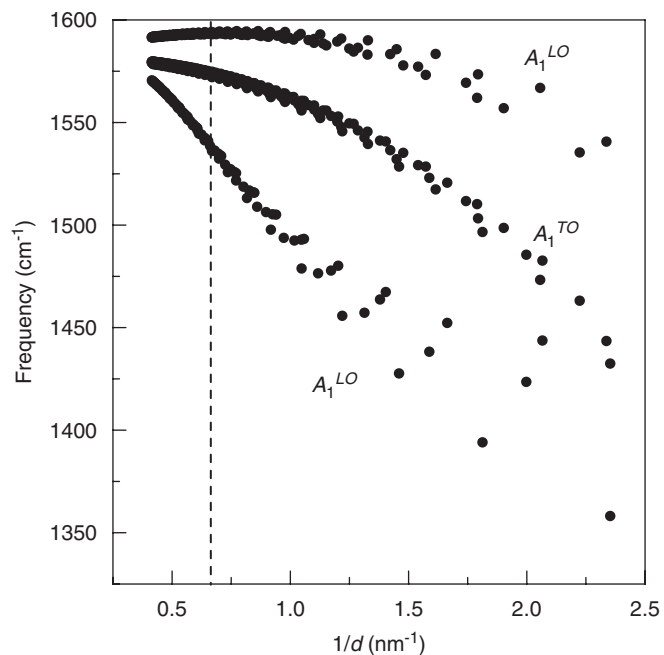


Fig. 2. The calculated frequency of the  $A_1$  G-band modes for all nanotubes as for Fig. 1. The data split into three strips due to (from top to bottom):  $A_1^{LO}$  phonons of semiconducting tubes,  $A_1^{TO}$  phonons of both semiconducting and metallic tubes, and  $A_1^{LO}$  phonons of metallic tubes. The data show chirality dependence given by  $\cos(3\theta)$  (not shown). For tube diameters of about 1.4 nm (dashed line), the observed G-band of the Raman spectra should consist of three subbands at about 1593, 1570, and 1540  $\text{cm}^{-1}$ . For smaller diameter tubes, the splitting between these subbands becomes larger.

phonons of S tubes,  $A_1^{TO}$  phonons of M and S tubes, and  $A_1^{LO}$  phonons of M tubes in order of decreasing frequency (see Fig. 2). The three sets of points give rise to three bands in the Raman spectra usually referred to as the  $G^+$ ,  $G^-(S)$ , and  $G^-(M)$  subbands. We find that, apart from the slight chirality dependence at small diameters, the three bands are described well by the expressions:  $\omega(G^+) = 1582 - 26/d^{1.7} + 38/d$ ,  $\omega(G^-(S)) = 1582 - 24/d^{2.2}$ , and  $\omega(G^-(M)) = 1582 - 433e^{-1.5d}$ . Ab-initio phonon calculations [10,11] predict similar splitting of the G-band. On the other hand, the analysis of Raman data reveals almost diameter-independent  $G^+$ -band and  $\omega(G^-(S)) = 1592 - 41.4/d^{1.4}$  [12],  $\omega(G^-(S)) = 1591 - 45.7/d^2$  [13], and  $\omega(G^-(M)) = 1591 - 79.5/d^2$  [13]. Our results and those of Ref. [10] correspond up to several  $\text{cm}^{-1}$  to the experimental ones except for our  $\omega(G^-(M))$  [14]. However, the assignment of the  $G^-(M)$  subband to  $A_1^{TO}$  phonons based on heuristic arguments [15] disagrees with our tight-binding results and the ab-initio ones [10,11].

We calculated  $J_{ii}$  of the RBM and the  $A_1$  G-band modes for the transitions  $E_{11}$  and  $E_{22}$  of metallic tubes and  $E_{22}$  of semiconducting tubes for all nanotubes in the diameter range 0.5–2.3 nm. The obtained data are plotted against  $1/d$  in Figs. 3–5. In the case of the RBM (Fig. 3), the  $J$ s can have positive or negative values. In some cases,  $J$  is close to zero and the intensity of the RBM of those tubes and transitions will be very small. For metallic tubes, the  $J$ s for  $E_{11}$  are larger than for  $E_{22}$ , in agreement with the Raman observation of the lower-energy component of the pairs of

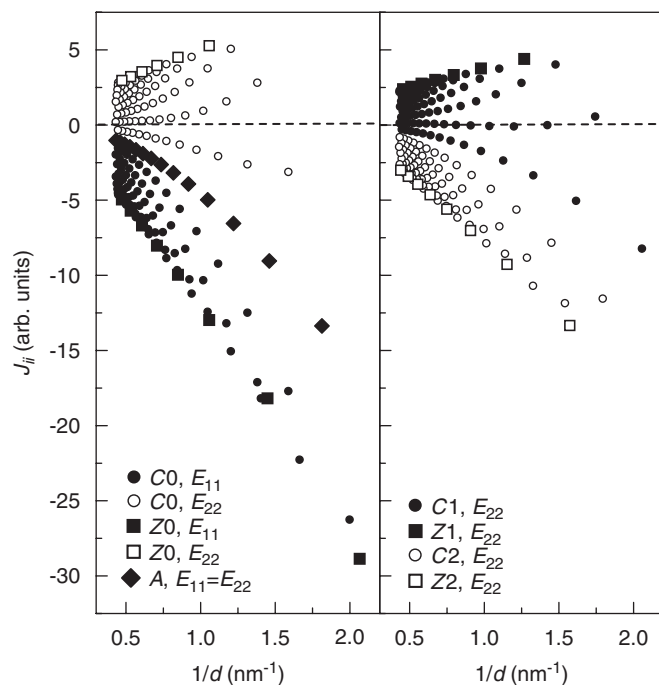


Fig. 3. The calculated  $J$  of the RBM for all nanotubes as for Fig. 1. The values of  $J$  can be positive or negative. They have large absolute values for the  $E_{22}$  transitions of Mod2 tubes and the  $E_{11}$  transitions of metallic tubes.

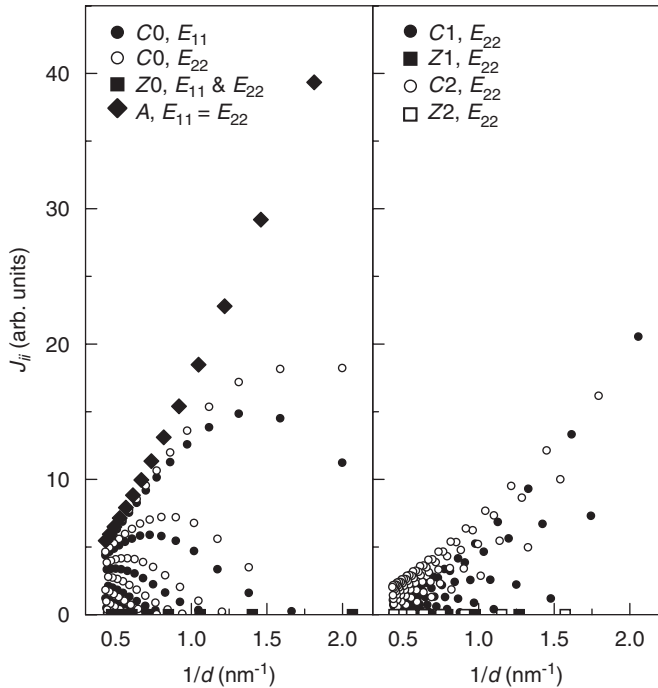


Fig. 4. The calculated  $J$  of the  $A_1^{\text{TO}}$   $G$ -band phonons for all nanotubes as for Fig. 1. All  $J$ s are positive. Zigzag tubes have  $J = 0$ , armchair tubes have largest  $J$ , and chiral tubes have intermediate values of  $J$ .

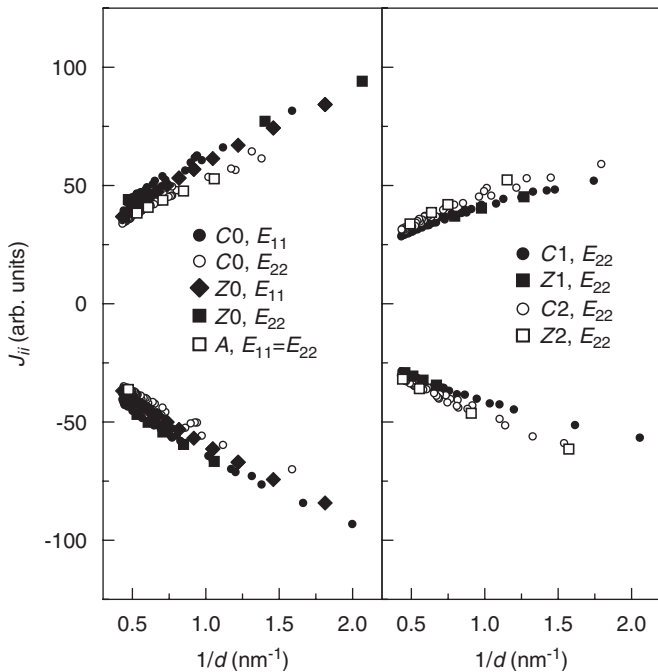


Fig. 5. The calculated  $J$  of the  $A_1^{\text{LO}}$   $G$ -band phonons for all nanotubes as for Fig. 1. The values of  $J$  can be positive or negative and lie on two strips. The  $J$ s for transitions  $E_{11}$  and  $E_{22}$  of metallic tubes have different signs, as well as those for  $E_{22}$  of Mod1 and Mod2 tubes. The closeness of  $E_{11}$  and  $E_{22}$  in metallic tubes can lead to high destructive interference and small Raman signal.

close optical transitions in such tubes. Similarly, for  $E_{22}$ , the semiconducting Mod2 tubes generally give rise to larger  $J$  than Mod1 tubes, in agreement with experiment [8,9].

With the increase of the tube diameter,  $J$  decreases to zero, because the corresponding mode in graphene, the lateral translation of graphene, is not Raman active. The chiral-angle dependence of  $J$  can be described well with a  $\cos(3\theta)$  factor.

The amplitudes  $J$  of the  $A_1^{\text{TO}}$   $G$ -band modes are positive for all tubes (Fig. 4). They are zero for zigzag tubes, where this phonon is not Raman active, and maximum for armchair tubes. The data for chiral tubes are between those for zigzag and armchair tubes. The  $J$ s for  $E_{11}$  and  $E_{22}$  of a given tube are close to each other, especially for metallic tubes. The values of  $J$  for the  $A_1^{\text{LO}}$   $G$ -band modes have different signs for  $E_{11}$  and  $E_{22}$  transitions of metallic tubes and the  $E_{22}$  transition of Mod1 and Mod2 tubes (Fig. 5). This alternating behavior is valid for other optical transitions as well. The closeness of the transitions  $E_{11}$  and  $E_{22}$  in metallic tubes can give rise to strong interference effects and can modify the Raman excitation profile, Eq. (16). Generally, the opposite signs for the two transitions of a given tube can cause a significant decrease of the Raman intensity in metallic tubes. The optical transitions of semiconducting tubes are relatively well separated, which rules out the possibility of such decrease and semiconducting tubes have normally high Raman signal for scattering from tangential  $A_1^{\text{LO}}$  phonons. The comparison between the results for the TO and LO modes shows that the latter have  $J$ s, which are almost an order of magnitude larger than that for the TO modes. As a consequence, the LO phonons will give much higher Raman intensity and their bands will dominate the Raman spectra.

Finally, we use the calculated phonon frequencies and Raman intensities to draw Raman maps (Raman intensity plotted against phonon frequency and laser excitation energy) of the RBM and  $A_1$   $G$ -band modes for a sample with well-dispersed nanotubes with a Gaussian diameter distribution with an average diameter of 1 nm and a standard deviation of 0.2 nm, typical for HiPCO samples. The following values of the parameters were used:  $\gamma_e = 0.03$  eV and  $\gamma_o = 6$   $\text{cm}^{-1}$ . Fig. 6 shows the Raman map for the RBM as a logarithmic contour plot. The map exhibits strips of lighter regions, corresponding to enhanced Raman intensities. Two of the strips, due to metallic and semiconducting tubes are marked with dashed lines. The lighter spots on the semiconducting strip arise mainly from Mod2 tubes with minor contribution from Mod1 tubes. The spots on the metallic strip arise mainly from  $E_{11}$  transitions with negligible contribution from  $E_{22}$  transitions.

Fig. 7 shows the Raman map of the  $A_1$   $G$ -band modes as a logarithmic contour plot. On this figure, one can clearly see three strips of lighter regions, denoted by dashed lines. The highest-frequency strip is due to  $A_1^{\text{LO}}$  phonons of semiconducting tubes and is almost independent of frequency for the presented energy range. The lower-frequency strip comes from  $A_1^{\text{TO}}$  phonons of both semiconducting and metallic tubes. It shows softening of the frequency with the increase of the laser energy, which

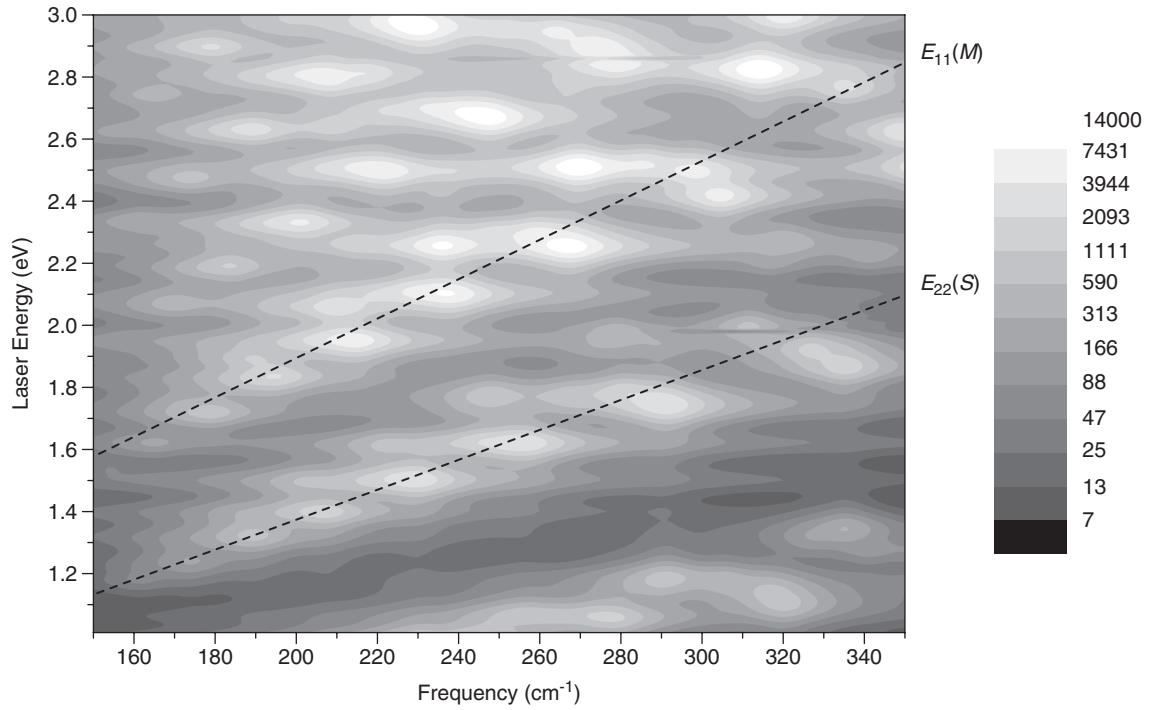


Fig. 6. The calculated Raman map of the RBM for a sample of nanotubes with an average diameter of 1 nm and a standard deviation of 0.2 nm. The contour plot shows the Raman intensity on a logarithmic scale. The lighter spots correspond to enhancement of the Raman scattering. These spots form strips arising from different transitions in semiconducting and metallic tubes. Two of the strips are marked with dashed lines.

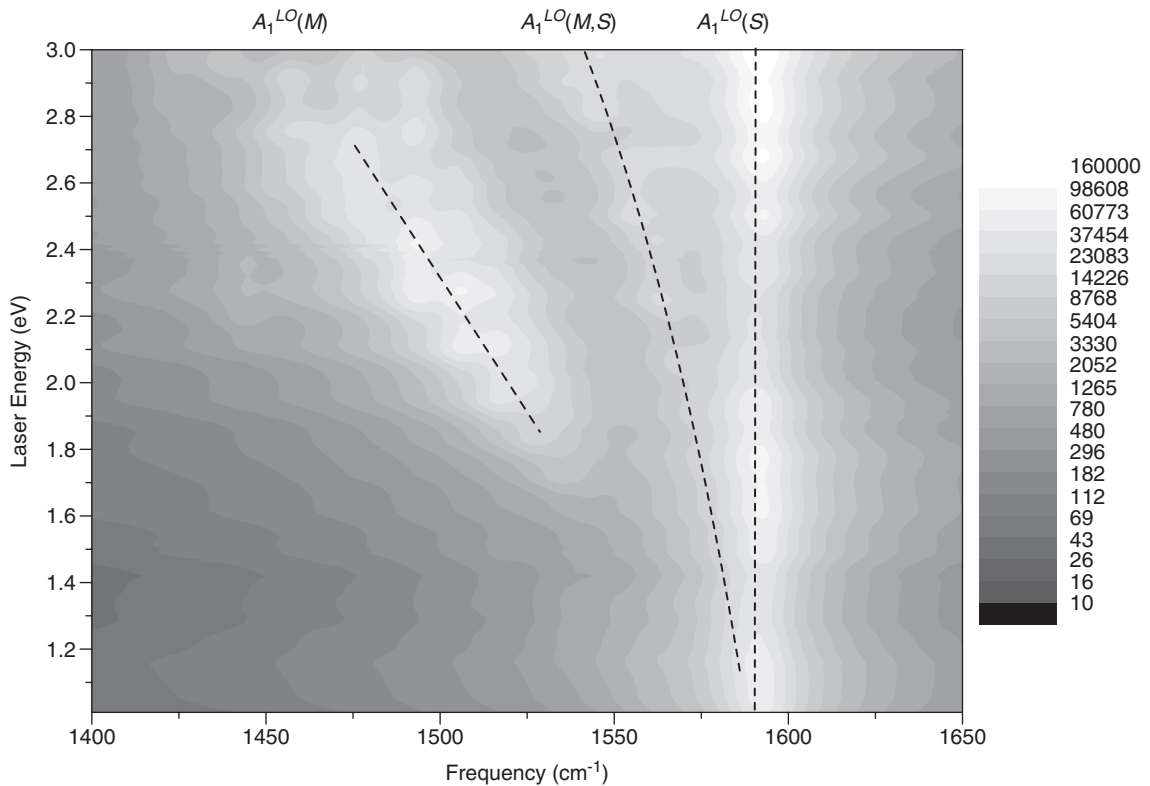


Fig. 7. The calculated Raman map of the  $A_1$  G-band phonons of the same sample as in Fig. 6. The three strips of lighter spots come from scattering from LO and TO phonons of semiconducting (S) and metallic (M) tubes, as indicated. The frequency of the two lower-frequency strips softens with the increase of the laser excitation energy.

corresponds to excitation of smaller-diameter nanotubes. The lowest-frequency strip arises from  $A_1^{\text{LO}}$  phonons of metallic tubes. We note that this strip extends in laser energies from about 1.9–2.8 eV, which corresponds to the  $E_{11}$  resonance windows for observation of metallic nanotubes with diameters around 1 nm. This strip shows softening with the increase of the laser energy as a geometric effect. Although this softening has been traditionally attributed to double-resonance processes [16,17], our results show that at least a part of it arises from the diameter and chirality dependence of the  $G$ -band frequencies. The comparison of the Raman intensity of the three strips shows that the  $A_1^{\text{LO}}$  one of semiconducting tubes is most intense followed down by that of metallic tubes, and the  $A_1^{\text{TO}}$  data. The present results correspond to previous theoretical estimations [10]. However, in the commonly adopted assignment of the  $G$ -band features, the lowest-frequency feature is ascribed to TO phonons because these phonons should be more diameter dependent than the LO ones [15]. Obviously, more theoretical and experimental work is necessary for clarifying this disagreement.

#### 4. Conclusion

We presented a symmetry-adapted approach to lattice-dynamical and electronic band structure calculations. This approach is exemplified in the case of a nonorthogonal tight-binding model. The results for the  $A_1$  zone-center phonon frequencies and their resonant Raman intensities are plotted against inverse tube diameter for practically all presently synthesized nanotubes. These results exhibit power-law diameter and  $\cos(3\theta)$  chirality dependence, which have to be taken into account in the characterization of nanotube samples by Raman spectroscopy.

#### Acknowledgments

VNP was supported by the Marie-Curie Intra-European Project MEIF-CT-2003-501080. This work was partly

funded by the Belgian Interuniversity Research Project on quantum size effects in nanostructured materials (PAI-IUAP P5/1).

#### References

- [1] J.C. Meyer, M. Paillet, Th. Michel, A. Moréac, A. Neumann, G.S. Duesberg, S. Roth, J.-L. Sauvajol, *Phys. Rev. Lett.* 95 (2005) 217401.
- [2] J. Maultzsch, H. Telg, S. Reich, C. Thomsen, *Phys. Rev. B* 72 (2005) 205438.
- [3] A. Jorio, C. Fantini, M.A. Pimenta, D.A. Heller, M.S. Strano, M.S. Dresselhaus, Y. Oyama, J. Jiang, R. Saito, *Appl. Phys. Lett.* 88 (2006) 023109.
- [4] C.T. White, D.H. Robertson, J.W. Mintmire, *Phys. Rev. B* 47 (1993) R5485.
- [5] V.N. Popov, V.E. Van Doren, M. Balkanski, *Phys. Rev. B* 59 (1999) 8355.
- [6] V.N. Popov, *New J. Phys.* 6 (2004) 17.
- [7] V.N. Popov, L. Henrard, Ph. Lambin, *Nano Lett* 4 (2004) 1795.
- [8] C. Fantini, A. Jorio, M. Souza, M.S. Strano, M.S. Dresselhaus, M.A. Pimenta, *Phys. Rev. Lett.* 93 (2004) 147406.
- [9] H. Telg, J. Maultzsch, S. Reich, F. Hennrich, C. Thomsen, *Phys. Rev. Lett.* 93 (2004) 177401.
- [10] O. Dubay, G. Kresse, *Phys. Rev. B* 67 (2003) 035401.
- [11] S. Piscanec, M. Lazzeri, F. Mauri, A.C. Ferrari, J. Robertson, *Phys. Rev. Lett.* 93 (2004) 185503.
- [12] A. Jorio, M.A. Pimenta, A.G. Souza Filho, Ge.G. Samsonidze, A.K. Swan, M.S. Ünlü, B.B. Goldberg, R. Saito, G. Dresselhaus, M.S. Dresselhaus, *Phys. Rev. Lett.* 90 (2003) 403.
- [13] A. Jorio, A.G. Souza Filho, G. Dresselhaus, M.S. Dresselhaus, A.K. Swan, M.S. Ünlü, B.B. Goldberg, M.A. Pimenta, J.H. Hafner, C.M. Lieber, R. Saito, *Phys. Rev. B* 65 (2002) 1555412.
- [14] The underestimation of the  $\omega(G^-(M))$  subband is due to the partial Coulomb screening used here. This problem has been discussed in detail in the literature (see, e.g., Bohnen et al., *Phys. Rev. Lett.* 93 (2004) 245501, Connetable et al., *Phys. Rev. Lett.* 94 (2005) 015503, Barnett et al., *Phys. Rev. B* 71 (2005) 035423, Lazzeri et al., *Phys. Rev. B* 73 (2006) 155426).
- [15] A. Jorio, A.G. Souza Filho, G. Dresselhaus, M.S. Dresselhaus, A.K. Swan, M.S. Ünlü, B. Goldberg, M.A. Pimenta, J.H. Hafner, C.M. Lieber, R. Saito, *Phys. Rev. B* 65 (2002) 155412.
- [16] J. Maultzsch, S. Reich, C. Thomsen, *Phys. Rev. B* 65 (2002) 233402.
- [17] J. Maultzsch, S. Reich, U. Schlecht, C. Thomsen, *Phys. Rev. Lett.* 91 (2003) 087402.